Multiscale Processes and Dynamics for the Monterey Bay Region Circulation

X. San Liang *

Harvard University, Division of Engineering and Applied Sciences, Cambridge, Massachusetts, USA

Allan R. Robinson

Harvard University, Department of Earth and Planetary Sciences and Division of Engineering and Applied Sciences, Cambridge, Massachusetts, USA

Abstract

The multiscale dynamics of the August 2003 Monterey Bay circulation has been investigated in an attempt to understand the complex processes underlying the highly variable ocean environment of the California coastal region. Using the rigorous general methodology of Multiscale Energy and Vorticity Analysis (Liang and Robinson, Dynamics of Atmospheres and Oceans, 38 (3-4), 195-230) the processes are reconstructed on three mutually exclusive time subspaces: a large-scale window, a mesoscale window, and a sub- mesoscale window. The ocean is found to be most energetic in the upper layers, and the mesoscale structures are primarily trapped above 200m. Through exploring the window- window interactions, we find that the dynamics underlying the complex surface circulation is characterized by a well-organized self-sustained bimodal instability structure: a Bay mode and a Point Sur mode which are located near the bay, and west of Point Sur, respectively. Both modes are of mixed type, but they are distinctly different in dynamics. The former is established when the prevailing upwelling wind relaxes, while the latter is directly driven by the upwelling winds. For both modes the wind instills energy into the ocean, which is stored within the large-scale window and then released to fuel mesoscale processes. Upon wind relaxation, the generated mesoscale structures propagate northward along the coastline, in a form with dispersion properties similar to that of an idealized free thermocline coastally trapped wave. We have also studied the deep layer flow, which is unstable throughout the experiment within the bay and north of the deep trench. We observe that the deep mesoscale flow within the bay may derive its energy from the sub- mesoscale window as well as the large-scale window. This study provides a real ocean example of how secondary upwelling can be driven by winds through nonlinear instability, and how winds may excite the ocean via an avenue different from the classical paradigms.

Key words: Multi-scale energy and vorticity analysis (MS-EVA),

1 Introduction

Monterey Bay is a crescent-shaped large embayment indented on the central California coast (Fig. 1). Distinguished by its high productivity and marine life diversity, it has become an important arena of interdisciplinary research. Oceanographers began to show their interests in this area as early as 1930 (Bigelow and Leslie, 1930). Since then continuing efforts have been invested to understand its circulation and dynamical processes, both as an integrated part of the California current system, and in its own right. Research along this line includes Bigelow and Leslie (1930), Skogsberg (1936), Shepard et al. (1939), Griggs (1974), Kelly (1985), Breaker and Mooers, 1986; Strub et al. (1987), Chelton (1988), Narimousa and Maxworthy (1989), Dewery et al. (1991), Breaker and Broenkow (1994), Rosenfeld (1994), Ramp et al. (1997), Collins et al. (2000), to name a few. During August-September 2003, a multi-institution multi-platform comprehensive experiment of observation and forecast, called AOSN-II (Autonomous Ocean Sampling Network - II), was conducted in this region. Densely covered data were collected and generated by a network of adaptive operational systems bringing together different sensors, robotic vehicles, and numerical ocean models. Many aspects of the project are discussed in other papers in this volume.

This paper studies the multiscale physical processes underlying the complex circulation during the AOSN-II experiment, and their relationship with the upwelling-related events. The multiscale complexity is one of the most prominent phenomena ever recognized in the Monterey Bay region. It is partly due to the changing external and internal forcings, partly due to the irregular domain geometry, and the interplay between the two. Winds, buoyancy flows, local heating, eddies, mixing, oceanic fronts, El Nino episodes, plus the curved coastline and the large submarine valley, all need to be taken into account for a faithful reconstruction of the processes as observed (Rosenfeld, 1994). The problem is therefore rather generic. It would be very difficult to rely on simplification of certain factors to gain a convincing understanding of the dynamics. Clearly, the complex configuration and the highly variable environment pose a great challenge to our study.

Liang and Robinson (2005a, 2005b, hereafter LR1 and LR2, respectively) have

* Harvard University, Pierce Hall G2H, 29 Oxford Street, Cambridge, MA 02138.
Email address: san@pacific.harvard.edu (X. San Liang).

developed a hierarchy of analysis methodologies to address this type of challenge. Their philosophy is: data-based geophysical fluid dynamics (GFD) theories may be developed independent of domain and other environment constraints, while numerical simulations can provide the data with arbitrary dynamic and geometric configurations. In this study, we present an application of their multiscale energy and vorticity analysis (MS-EVA), which deals with nonlinear and intermittent oceanic processes on a generic basis.

The paper is organized as follows: We first give a brief introduction of the MS-EVA and MS-EVA-based finite-amplitude localized instability analysis, followed by a short account of the dataset generated from the AOSN-II simulation. The analysis starts in section 4, where we show how a large-scale window, a mesoscale window, and a sub-mesoscale window are demarcated based on simulated time series. The MS-EVA is set up in section 5. Processes are then projected on the three scale windows, and the synthesized features are described in section 6. In sections 7 and 8, we focus on how kinetic energy and potential energy are transferred from the large-scale background to mesoscale eddy structures. Particularly, section 7 gives a detailed analysis for the baroclinic and barotropic instabilities associated with the variation of the prevailing winds. In section 9, we extend the analysis to the sub-mesoscale window, and substantiate the multiscale dynamics inference with some observations from the simulated fields. This study is summarized in section 10.

2 Multiscale energy and vorticity analysis (MS-EVA) and MS-EVA-based localized instability analysis

The research methodologies for this study are the localized multiscale energy and vorticity analysis (MS-EVA) developed in LR1, and the MS-EVA-based theory of baroclinic and barotropic instability (LR2). MS-EVA has been used in the study of the dynamics of a previously identified process, the meandering of the Iceland Faeroe Front (IFF) (LR3); in this paper, we show how it can be adopted to investigate an area where the characteristic process is previously unclear.

MS-EVA is built on the basis of a functional analysis machinery called multiscale window transform (Liang, 2002, chapter 2). In this framework, a function space is decomposed into a direct sum of several mutually orthogonal subspaces, each with an exclusive range of time scales. Such a subspace is termed a *scale window*. Our research task is, in an abstract way, to represent ocean processes on appropriate scale windows, and then to study how these processes evolve and interact through exploring the window-window interactions. In this context, we need a large-scale window, a mesoscale window, and a sub-mesoscale window (denoted as $\varpi = 0, 1, 2$ respectively). Theoretically,

demarcation of these windows does not require a basis, but for simplicity we appeal to wavelet analysis to fulfill it, as in LR3. This yields three "window bounds": j_0, j_1, and j_2, which are the wavelet scale levels marking the upper bounds of large-scale, mesoscale, and sub-mesoscale windows, respectively. In other words, given a time series scaled with its length, 2^{-j_0}, 2^{-j_1}, and 2^{-j_2} are the lower time scale bounds for the three windows.

MS-EVA deals with multiscale dynamics through exploring the energetics on the specified scale windows. For a geofluid flow, the kinetic energy (K_n^ϖ) and available potential energy (A_n^ϖ) grow as, in a symbolic form (horizontal dissipation/diffusion ignored),

$$\dot{K}_n^\varpi = \Delta Q_{K_n^\varpi} + \Delta Q_{P_n^\varpi} + T_{K_n^\varpi} - b_n^\varpi + F_{K_n^\varpi,z}, \tag{1}$$

$$\dot{A}_n^\varpi = \Delta Q_{A_n^\varpi} + T_{A_n^\varpi} + b_n^\varpi + F_{A_n^\varpi,z}, \tag{2}$$

on window ϖ ($\varpi = 0, 1, 2$) and at time step n, where the ΔQ-terms represent the multiscale transport process on the specified scale window ϖ, and the "T-terms" are *perfect transfers* among different windows in the sense that they vanish when averaged over ϖ and n. In the equations, the symbol $\widehat{(\cdot)}_n^{\sim\varpi}$ indicates a multiscale window transform (LR1, Sec. 2) on time window ϖ and at times n. Other notations are summarized in Table 1. Note all these terms are horizontally treated with a two-dimensional large-scale window synthesis (LR1, section 7).

The major difference between Eqs. (1) and (2) and the classical formalism lies in that all the terms here are in a 4D field form, and hence intermittent processes are naturally embedded. Amongst these terms, of particular importance are the nonlinear perfect transfers (T), which connect processes between different scale windows. It has been shown that these transfers are closely related to the classical GFD stability, and the classical hydrodynamic stability theory in the sense of Lyapunov (LR2). A localized hydrodynamic instability analysis was henceforth rigorously established, which we here give a brief review.

Consider first a system with only two windows involved (window 0 and window 1). Its stability can be explored either with a large-scale window, or a mesoscale window, depending on which window you are in when viewing the problem (except for the opposite sign). This makes sense, as stability/instability is related to the transfers between two windows. In LR2 and LR3, Liang and Robinson introduced the theory based on the mesoscale window, in this study we adopt the other stance to express it. Let

$$BC = T_{A_n^0}^{0\to 1} = -T_{A_n^0}^{1\to 0}, \tag{3}$$

where the superscript $\varpi_0 \to \varpi_1$ ($\varpi_0, \varpi_1 = 0, 1$) denotes an interaction analysis

operator that selects out the transfer component from window ϖ_0 to window ϖ_1 (see LR1, Sec. 9), and

$$BT = T^{0\to 1}_{K^0_n} = -T^{1\to 0}_{K^0_n}. \tag{4}$$

This definition of BC and BT differs from that in LR2 and LR3 in that we are considering $T^{0\to 1}_{A^0_n}$ instead of $T^{0\to 1}_{A^1_n}$, and $T^{0\to 1}_{K^0_n}$ instead of $T^{0\to 1}_{K^1_n}$ (note the difference in subscripts). The two formulations need not be the same, but they are equivalent on the large scale window according to the property of perfect transfer (cf. LR1). For this particular problem where no *a priori* process is specified, the advantage of Eqs. (3) and (4) over those used in LR3 for the IFF meandering is that (3) and (4) allow one to stand on a larger scale to view the problem and therefore to get the basic physics upfront which would be otherwise very complicated to perceive.

The criterion of instability analysis based on (3) and (4) is the same as that of LR2 and LR3. Specifically,

(1) A flow is locally unstable if $BT + BC > 0$ and vice versa;
(2) For an unstable system, if $BT > 0$ and $BC \leq 0$, the instability is then barotropic;
(3) For an unstable system, if $BC > 0$ but BT is not, the instability is baroclinic;
(4) If both BT and BC are positive, the system is undergoing a mixed instability.

For convenience, BT and BC may also be loosely referred to as barotropic transfer and baroclinic transfer, respectively.

The above instability analysis may be carried down to the transfers between the mesoscale and sub-mesoscale windows. All the criteria are the same expect a replacement of $1 \to 2$ for $0 \to 1$. In the three-window case, if the energy source is ultimately traced to the basic background, the nonlinear perfect transfer between the large-scale and mesoscale windows can be viewed as a primary instability, while that between the mesoscale and sub-mesoscale windows is a secondary instability. To avoid confusion, we only assign the shorthands BC and BT to the former. When a secondary instability is concerned, the full expressions $T^{1\to 2}_{A^1_n}$ and $T^{1\to 2}_{K^1_n}$ will be written out.

3 Dataset

In August-September 2003, a multi-institution collaborated multi-platform survey, including the deployment of two fleets of AUVs,[1] was conducted in the Monterey Bay region in a domain as shown in Fig. 1. It comprises of five cruises, which respectively last from 2 August through 6 August (Model initialization and start of science experiments), 7 August through 20 August (Science experiments and model skill assessment), 21 August through 25 August (Model re-initialization, and continued science experiments), 26 August through 2 September (Science experiments and model skill assessment), and 3 September through 7 September (Model skill assessment and final science experiments). Data are collected and taken into numerical models as input to reconstruct the whole circulation. In this study, the output from the Harvard Ocean Prediction System (HOPS) is chosen for our analysis.

We use a well validated reanalysis output to form the dataset.[2] The research domain is horizontally discretized into a 83×96 mesh grid, with an equal grid spacing $\Delta x = \Delta y = 1.5$ km. In the vertical direction a double sigma coordinate is adopted. Data of external forcing are derived from the COAMPS atmospheric fields and objectively mapped onto the grid. The nowcast/forecast starts on August 2, initialized with the climatology, with data taken in every day at noon upon availability until the initialization survey is completed. The model is fully initialized as of August 6. We label this day as day 1 for reference convenience. Sequentially August 7 through September 7 are called day 2, day 3, and so forth. For details, refer to Haley et al. (2005) and Lermusiaux (2005).

Winds play a dominant role in the upwelling process in this region (e.g., Rosenfeld et al., 1994). Shown in Fig. 2 are the stickplots of the wind at Mooring station M1 (36.755°N, 122.025°W). During the experiment period, the maximal magnitude of the upwelling favorable wind is attained on August 11. It relaxes on August 18 - 23. After that, another cycles starts and a second peak appears around August 27.

We focus on the processes between these two wind stress peaks. Time sequences of temperature and flow for depths 10 m and 150 m are shown in Fig. 3. These two depths are typical of the processes in the surface layer and the deep layer, respectively. It is not our intention to give them a complete description, but from these plots it is easy to identify some features with dynamical significance. As is clear, the surface distribution is very complicated

[1] See David Fratantoni: http://glider.whoi.edu/dmf, and
Russ Davis: http://www-pord.ucsd.edu/∼rdavis.

[2] Wayne Leslie and Patrick Haley: http://people.deas.harvard.edu/∼leslie/AOSNII/index.html, http://people.deas.harvard.edu/∼haley/Work/HOPSreal_time.html.

and much affected by the wind. There are two cold centers along the coast, one residing offshore Point Sur, another one between the bay and offshore Point Ano Nuevo. When the wind relaxes, warm water quickly takes over, in agreement with previous observations (e.g., Rosenfeld et al., 1994). But the most intensive upwelling occurs outside Point Sur and the bay mouth on August 19, the day when the wind has just relaxed. In contrast, the deep layer is less affected by the winds and the processes seem to be simpler. Warm patches appear all the time outside Point Sur and within the bay, and propagate northwestward along the coast, regardless of the winds. Toward the end of this work, we expect to give these observations a satisfactory explanation.

4 Spectral analysis and window bound determination

As in LR3, the window bounds needed for the MS-EVA analysis are determined through wavelet spectral analysis of point time series. We have examined the following six points for this purpose (cf. Fig. 1): point 1: (65, 40); point 2: (30, 15); point 3: (60, 45); point 4: (60, 80), point 5: (55, 30), point 6: (45, 50). These points are typical of the geography and certain dynamical processes observed in the simulation. Specifically, point 1 and 3 are at the mouth of the bay, and the latter is also over the canyon at the outer bay; point 2 is in a very energetic region; points 4 and 5 are located offshore Point Ano Nuevo and Point Sur, the two crucial places in dynamics, while point 6 is within a large surface anticyclonic eddy observed most of the time through the experiment. As surface upwelling events are of special interest for this region, we focus on processes in the upper layers. To facilitate visual inspection, the means have been subtracted from all the time series before plotting the spectra.

For this region, we have observed that temperature resembles density anomaly in spectrum. Temperature hence characterizes well the available potential energy distribution. We have also found that points 3 and 5 are typical of the six chosen temperature series. Contoured in Fig. 4 are their respective spectra. In both of them there is an obvious transfer of energy from low scale levels (large scales) to higher scale levels as time moves on. The transfer starts on day 8 or August 14, and is enhanced from day 12 through day 16 (August 18-22), which is the wind relaxation period. At point 3, there is a strong transfer on day 16 to a mesoscale event from both large scales and smaller scales, forming a very clear maximum at scale level 2 (8 days). All these events are related to the wind relaxation.

A similar trend is also seen on the velocity spectra. Points 4 and 5 are found to be two typical points. (Point 3 is similar to point 4, but with features not enhanced as that of point 4.) Shown in Fig. 5 are the spectra for u at these two points. Again, the energy transfer is clearly seen, but the timing

differs. At point 4, it begins on day 8 (August 14), gets enhanced on day 16, and lasts through day 24 (August 30). The peak takes place at scale level 2, corresponding to a period of 8 days. At point 5, the transfer period is from day 12 (August 18) through day 20 (August 26), and the maximum is at scale level 3 (4 days).

According to the above analysis, if one focuses on the relaxation events, both the temperature (density anomaly) spectra and the velocity spectra support a time window partitioning with $j_0 = 2$ and $j_1 = 5$. That is to say, processes with scale levels smaller than 2 should be included in the large-scale window, while those higher than or equal to 5 are left for the sub-mesoscale window. Sensitivity study has been performed and we observe that the resulting MS-EVA analysis is very robust around this set of parameters.

As regards the spatial scale window used for the horizontal filtering, the window bound (denoted as $j_0^{\rm sp}$) choice is found insensitive once the time window bounds are appropriately set. This is just as we observed in LR3. Specifically, the results with $j_0^{\rm sp} > 5$ are almost quantitatively identical to the results with $j_0^{\rm sp} = 5$; when $j_0^{\rm sp}$ lies below 5, the results are still qualitatively the same, except that the lower the $j_0^{\rm sp}$, the more damped the variation. We thereby choose $j_0^{\rm sp} = 5$, which corresponds approximately 11 km in length.

5 MS-EVA setup

In the MS-EVA formulation, flat z-coordinates are used. The double sigma coordinate adopted in the HOPS forecast must be interpolated onto flat levels before the MS-EVA application. The z-levels chosen are summarized in Table 2. We select depths 0 m, 10 m, 30 m, 150 m, and 500 m for our analysis. Among them, depth 10 m is within the mixed layer (either the top, middle or bottom depending on the winds), depth 30 m lies in the middle of the thermocline, depth 150 m is roughly at the bottom of thermocline and in the core of the California undercurrent, while depth 500 m cuts across the deep California current system (see Haley et al., 2005). The necessary fields are linearly interpolated onto these levels.

A mean profile of $\bar{\rho} = \bar{\rho}(z)$ is needed for the available potential energy analysis. The mean is computed through taking average of ρ over all the available data points and time instants from the simulation. The resulting profile is plotted in Fig. 6. In a brief summary, these parameters are listed in Table 2.

6 MS-EVA analysis: Description of fields

With the parameters in Table 2, it is straightforward to reconstruct features on the prescribed scale windows. This section gives a description of these multiscale features. The governing dynamics will be presented in the next section.

6.1 Temperature

Understanding the temperature distribution and its variation in response to the upwelling-favorable wind is a major goal for the Monterey Bay circulation study. The response is reflected on different time scale windows. Fig. 7 presents a sequence of the large-scale reconstructions of temperature for levels 2 and 12. In the upper layer, a belt of cold water dominates along the coastline. The upwelled water is organized into two cold centers: one within the bay, another outside Point Sur. This horizontal structure is most conspicuous around August 15, and becomes weakened through the end of the month. In contrast, the interior region is characterized by a large pool of warm water. As time goes on, the pool gets enlarged and eventually takes over the whole western part of the domain at depth 10 m.

There is a distinct vertical structure on the large-scale temperature field. In deep layers, the water is generally warmer along the coastline and colder seaward, as shown in Fig. 7c. The trend reversal of offshore temperature gradient occurs roughly at 100 m (figure not shown).

The mesoscale temperature is rich in structure and process. This is particularly so in the surface layers. Shown in Fig. 8 is the mesoscale temperature evolution at level 2. Three major events are clearly seen during the period day 6 (August 11) through day 22 (August 27). On day 6, a dipole shows outside the bay, with warm water in the south. There is no evidence that this dipole propagates. Rather, it grows and oscillates in time, with shape changing accordingly. On day 14 (August 19) it reaches its minimum in low temperature, and on day 18 (August 23) the phase is reversed, implying a period of 8 days for this process. As a result, a large pool of cold water appears in the middle of the domain on August 19. Comparing to Fig. 3 and Fig. 7, the sudden cooling of water on this day should be a secondary upwelling. We shall come back to this issue later on in the MS-EVA analysis.

A new structure begins to emerge north of the bay outside Point Ano Nuevo on day 12, which becomes evident by day 14 (August 19), and strong enough on day 16 (August 21) that it since then propagates northward along the coast, with a period of about 8 days. The third event is found on August 13 as a

dipole near the southwestern corner, with a cold center to the left. This dipole keeps growing until the wind relaxes, when it begins to propagate northward on August 21. The patterns of August 25 and August 21 are approximately out of phase, implying this event also has a period of roughly 8 days and a wavelength 60 km, which implies a speed of 0.08 m/s. We have computed a coastal trapped wave (CTW) properties with the averaged buoyancy frequency profile and topography for this region (see Appendix A). This observation agrees with a thermocline-trapped CTW mode with an eigenvalue (inverse of phase speed) 11 s/m.

There is also a vertical structure on the mesoscale field. A distinct feature is that the mesoscale variation amplitude decreases with depth. A decreasing trend is also seen on the horizontal scale, as shown in the distributions for depth 10 m (Fig. 8), and that for depth 150 m (Fig. 9) where processes of much smaller scales dominate. Below 250 m, mesoscale variations give away to sub-mesoscale processes.

The processes in deep layers are relatively simple. At level 12 (150 m), we see cold and warm pools being alternatively generated within the bay, and propagating northward along the coast. Comparing the patterns of August 19 and August 23, the period is also roughly 8 days, and its wavelength approximately 60 km, with a speed of 0.08 m/s. That is to say, the deep layer mesoscale structure also propagates in a way similar to the free CTW mode as computed in the Appendix.

6.2 Velocity

The flow field is also rich in scale. Fig. 10 shows the large-scale reconstructions for levels 2 (10 m) and 12 (150 m). They are typical of the flows for the surface layers and deep layers. At level 2, the flow is a little complicated due to the direct influence of winds. Roughly it can be classified into two types: one coastal current flowing southward, one northward current offshore pertaining to the California Counter Current (CCC). But this trend is interrupted by a cyclonic gyre outside Point Sur. For the deep layers, the flow pattern is much simpler. The whole system is characterized by a strong northward along-slope current, with a weaker California Under Current to the left. The general trend of the large-scale current is getting weaker toward the end of August.

On the mesoscale window, the flow exhibits itself in a complicated pattern in upper layers, particularly in surface layers (Fig. 11). In the 10-m sequence, the strength of variability does not change much until the wind relaxation (cf. the distribution of August 17 or day 12 in the figure), when a burst of variability appears which lasts toward the end of the month. Eddy structures

are generated, advected, and diminished here and there, making the flow a very complex system. We will return to the analysis later with more powerful methodologies.

The deep layer variability is relatively simple. Drawn in Fig. 12 is a sequence of the 150-m mesoscale flow. Generally, the variability is in the form of a dipole outside the northern part of the bay. The variability keeps being generated near the bay area during August 11 through August 23 (days 6-18). It then propagates northward, becomes weakened and finally disappears just near the northern boundary. It may be summarized as a source outside the bay, plus a sink near the northern boundary. On August 19 (day 14) and August 23 (day 18), the patterns are roughly out of phase, implying a period of about $4 \times 2 = 8$ days. One may also measure the wavelength from the pattern of August 23 (day 18) to be 60 km. This gives a speed of about 0.08 m/s, close to the free CTW mode described above. In addition to the major feature, there is also a process occurring near the southwestern corner. A cyclonic eddy and an anticyclonic eddy appear alternatively as time goes. The amplitude increases but no propagation is identified. Underlying there could be a local instability. We will see more details of dynamics later.

6.3 Multiscale energy

Multiscale energy distributions could reveal more information about the ocean response to the external forcing. As we will see later, the effect of winds enters the energy balance mainly through the large-scale window. For this reason, we first look at the large-scale energy and its variation.

At depth 10 m, the large-scale potential energy (Fig. 13, upper panel) exhibits its features in two regions: One lies mainly in the bay, another off Point Sur. Both regions see APE increases as time moves on from August 11 to August 15, when their maxima are attained respectively, and then decreases toward the end of the month. Note that sometimes the hotspot within the bay extends northward to Point Ano Nuevo.

A similar structure also exists on the surface layer large-scale KE sequential maps (Fig. 13, lower panel), and their variations also follow a similar trend. The difference is that the southern counterpart lies far offshore, and it becomes strengthened again after the relaxation period (August 18 - 23). Another difference is that there is a third hotspot located in the northwest. It is strongest on August 11 during the period under concern. We will see in the next section that underlying this KE hotspot the dynamics is completely different from the other two.

The deep-layer large-scale energy reveals a different pattern of distribution.

Drawn in Fig. 14 is the large-scale APE and KE of August 15 for depth 150 m. Obviously the flow stores its APE (left panel) on the coastal side and in the northwestern corner, while kinetically it is most energetic along the shelf-break. The largest kinetic energy occurs on August 11. It decreases afterwards through the survey period (figure not shown).

6.4 Bay mode and Point Sur mode

In the above we have identified two large-scale energy centers in the surface layer which vary in some related pattern as the wind applies (Fig. 13). A significant part of the kinetic energy, and almost all the potential energy, are organized into such a structure. One may use the term "mode" to describe this structure. But it is not a mode by traditional definition, as the two centers do not covary in response to the applied forcing. Nonetheless, we may as well regard the two centers as two distinct modes, i.e., two localized modes in the framework of our localized analysis. We will henceforth refer to them respectively as the *Bay mode*, and the *Point Sur mode*, depending on where they are. Notice the Point Sur mode does not coincide in location on the APE map and the KE map. In the next section we will see that it is more consistent with respect to their driving forces, the perfect transfers.

7 MS-EVA analysis: Barotropic and baroclinic transfers

The multiscale processes are governed by multiscale dynamics. In this section, we focus on the interaction between large-scale and mesoscale windows, which is measured by two field metrics, the barotropic transfer and baroclinic transfer, or BT and BC for short. These metrics have been connected to barotropic instability and baroclinic instability in a generalized sense (cf. section 2).

7.1 Surface layers

As is shown in the preceding section, the dynamics of the upper layer is relatively complex. We calculate its BT and BC distributions to distinguish intrinsic mechanisms from extrinsic mechanisms. Again, level 2 (10 m) is found typical of the upper layer in this regard. Figs. 15 and 16 depict how BC and BT evolve with time on this level.

Look at BC first. A remarkable feature is its bi-modal structure: Clearly shown in the sequence of Fig. 15 are two positive BC centers. We look at the southern one first. Starting from August 11, it emerges in the domain outside Point

Sur. It becomes stronger as time goes on and reaches its maximum on August 15. After that, the transfer strength decreases until August 19 when it splits into two parts. The upper part eventually merges into another center further north which we will describe soon. The bottom part rejuvenates after August 23. This BC hotspot correlates well in variability to the Point Sur mode on the large-scale APE maps (Fig. 13), except that the Point Sur mode of APE sticks tight to the coastline. Notice positive BC means loss of energy to the mesoscale window. So the correlation between BC and the large-scale APE indicates that the wind stores energy in the large-scale window, and then releases it to mesoscale processes. On the other hand, the discrepancy in location between them implies that the energy could be first built up near Point Sur, then advected westward and is finally released. This scenario will be clear in section 8.1.

Another positive center on the sequential maps is located between the Bay and Point Ano Nuevo. In comparison to the Bay mode on the maps of Fig. 13, the location is a little northward. But for convenience we will still refer to it as the *Bay mode*—it gives rise to the Bay mode of APE, as we will see in section 8.1. This mode does not emerge until August 15, when the wind slows down. It reaches its maximum on August 21, and becomes weakened afterwards.

Both the two BC hotspots are highly correlated with the wind during the major time of event. The Point Sur mode generally follows the wind stress variation, with a phase lag of 2-3 days. In contrast, the Bay mode has a negative correlation with the wind. The signs of correlation indicate that the two baroclinic instabilities are triggered through different mechanisms. This will be clear soon.

The opposite correlations with the wind and hence the relative variation between the two modes suggest some kind of relation between the two transfer centers. It is not clear whether this means a conservation law while the two modes interact. But we do observe interactions between them, and particularly interactions are observed during the relaxation period. They are marked by the the splitting of the Point Sur mode, which should exchange energy and information as well.

On the BT maps (Fig. 16), there is also a bi-modal structure, and a similar evolution pattern is observed. The difference between BT and BC is that the two modes of BT are located a little southward and eastward before the wind relaxes, and that the Point Sur center becomes negative during the relaxation period. In this case, the "Bay mode" is really within the bay before August 17, but the Point Sur mode is far from the coast. The correlations of the two centers with the wind are also in opposite, just as that on the BC maps.

Although BC and BT follows a similar variability pattern with the wind,

the wind influence seems to be more conspicuous on the BT evolution. In the south, negative transfer appears in the vicinity of the southwestern corner during August 18-23; in the middle, the hotspot jumps from within the bay on August 17 to where the BC Bay mode resides. Both these prominent variabilities occur in response to the wind relaxation, indicating a closer relationship of BT to external forcing.

The BC and BT distributions show that the system is unstable in the upper layer within the bay after August 11, because BC+BT is positive (cf. Fig. 17), and the instability is of a mixed type. The most unstable case occur during the relaxation period, August 18 through 23. Off Point Sur, the flow is also unstable except for the relaxation period, and the instability is also of a mixed type. But it is dominated by baroclinic instability before August 18, and switched to barotropic instability after August 23. During the relaxation period, the flow tend to be stablized outside Point Sur. The high correlations of BT and BC with the wind indicate that these instabilities are to a large extent triggered externally. The whole story will be clear after a deeper study of the energetics.

7.2 Deep layers

The deep layer transfer patterns are much simpler than their surface counterparts. Shown in Fig. 18 are the BC (left panel) and BT (right panel) on August 15 for the depth 150 m. On the BC map, the whole domain is characterized by a positive center within the bay, and a weak negative center to the west of Point Sur. All the rest regions are virtually zero in transfer. This simple distribution keeps its structure through the whole experimental period, though the hotspot gets weakened, and the negative center disappears during relaxation (figures not shown).

The 150-m BT and its evolution is also simpler than the surface BT. In the right panel of Fig. 18, it is basically composed of three distinct centers: a positive hotspot in the middle, a negative center to the north, and another weaker positive center to its south. The southern center varies in a way similar to the Point Sur mode at depth 10 m as shown in Fig. 16, and also becomes negative when the wind relaxes. The northern center is always negative, forming a sink to certain perturbations. This is consistent to what we have observed in the m flow plots (Fig. 12).

What worths special attention is the middle hotspot. It exists from August 12 to August 23, and does not vary much during the period, both in strength and location. Clearly it does not show correlation to the wind. If we compare it to the topography in Fig. 1 and the flow in Fig. 10, it sits just downstream

of the deep canyon. It appears to be caused by the California Under Current flowing over the canyon, a mechanism distinctly different from that of other positive centers.

8 MS-EVA analysis: Energy balance

We have examined the baroclinic and barotropic transfers during the large-meso-scale interactions, and explored the correlation between these transfers and the wind stress. In this section, we study the other MS-EVA terms in the energy balance. As it is observed that the external forcing enters the equation mainly through the large-scale window, we consider the large-scale MS-EVA only.

8.1 Point series

We first choose two locations, S: (30,15), and B: (57,55), to study the problem (see Fig. 17). These locations are associated with the two distinct transfer centers over the experimental period. For convenience, we refer to them as S ("Sur") and B ("Bay"), respectively.

Plotted in Fig. 19 is the point series of the large-scale MS-EVA terms at point S. One observation is that external forcing contribution ($F_{A_n^0,z}$) dominates the balance. Another observation is that buoyancy conversion (b_n^0) is rather weak. Balancing the work due to the external forcing is mainly from the horizontal advection in the APE equation ($\Delta Q_{A_n^0,h}$), and the horizontal pressure work in the KE equation ($\Delta Q_{P_n^0,h}$). The importance of other terms varies with time and location, but in the APE plot external forcing ($F_{A_n^0,z}$), advection ($\Delta Q_{A_n^0,h}$), and baroclinic transfer ($T_{A_n^0}$) dominate the balance throughout the duration of the experiment.

The simple balance between $\Delta Q_{A_n^0,h}$, $F_{A_n^0,z}$ and $T_{A_n^0}$ offers an explanation about the discrepancy we have observed between the locations of BC and APE for the Point Sur mode (cf. the August 15 map in Fig. 13 and Fig. 15). The positive correlation between $F_{A_n^0,z}$ and $T_{A_n^0}$ and the negative correlation between $\Delta Q_{A_n^0,h}$ and $T_{A_n^0}$ indicate that the energy transferred to the mesoscale eddies is not from the *in situ* large-scale energy instilled by the external forcing, but from its neighborhood via advection. Clearly, large-scale energy is first built up near Point Sur. It is transported westward by some distance, and then transferred to the mesoscale window through an instability, leading to the generation of mesoscale eddies.

It merits mentioning that both the baroclinic transfer and the barotropic transfer make significant contributions to their respective equations. As we note before, our BC and BT are equal to $-T_{A_n^0}$ and $-T_{K_n^0}$ followed by an interaction analysis which selects out the part from large-scale window to the m window (indicated as superscript $0 \to 1$ in the text). The variations of $T_{A_n^0}$ and $T_{K_n^0}$ then from an aspect reflect the BC and BT, except for a negative sign. Since we have seen that energy does not convert much between the two types, these transfers are the main indices for the temperature fluctuation and flow variability, respectively. In this sense, although the instability has a ingredient of baroclinicity, it is not Eady-like, as the buoyancy conversion is rather weak.

The correlation between the external forcing and the transfers is clearly seen from the plots. In Fig. 19a, the transfer strength is positively correlated to $F_{A_n^0}$ with high correlation. Particularly, $-T_{A_n^0}$ reaches its maximum just a couple of days after the $F_{A_n^0}$. (Recall that related to instability is negative $T_{A_n^0}$.) The same observation is made in Fig. 19b before August 23, when the wind relaxes. The largest negative value of $T_{K_n^0}$ occur on August 13, while on the same day the wind instills the largest part of energy into the ocean. When the wind relaxes, the transfer becomes positive, i.e., the flow is stablized, in agreement with our previous observation with the BT sequence. After August 23, this region experiences another instability, but the driving mechanism seems to be changed. Nonetheless, one can safely say that the Point Sur instability mode is directly driven by the external forcing.

For Point B which is with the Bay mode, the energetic scenario is similar with the APE equation. The most significant balance is still between the external forcing, the horizontal advection and the baroclinic transfer, and the variation trends of the three also take resemblance to Fig. 19. Following the same argument as that of Point S, we may explain away the location discrepancy between the BC center and the APE center of the Bay mode (cf. Figs. 15 and 13): The Monterey Bay provides the necessary energy for the BC center and has it established outside Point Ano Nuevo when the wind relaxes.

But the Bay mode KE equation is a little different: The balance is between horizontal pressure work and the work done by winds together with vertical pressure force. Especially different is the correlation of the transfers to the external forcing work. In Fig. 20a, $T_{A_n^0}$ almost vanishes when the absolute value of $F_{A_n^0}$ reaches its peak on August 14-15, while $-T_{A_n^0}$ is maximized as wind relaxes. Same thing is shown in Fig. 20b. $T_{K_n^0}$ takes its significant negative value from August 17 to August 25, which correspond to the valley of the curve of $F_{K_n^0}$. Clearly, the instability mode at point B has a driving mechanism completely different from that of point S. It is the relaxation of winds that makes this region unstable.

8.2 Horizontal MS-EVA maps

We now look at the horizontal maps of the major MS-EVA terms. In Fig. 21, the most significant two terms in the APE balance are contoured for August 15. Observe the two negative centers on the map of vertical APE diffusion ($F_{A_n^0}$). They correspond well in location to the two instability modes we have discussed above.

The KE balance is mainly between horizontal pressure working rate $\Delta_h Q_{P_n^0}$, vertical pressure working rate $\Delta_z Q_{P_n^0}$, and the wind stress working rate $F_{K_n^0}$. We have seen from Fig. 20 that the three correlate well to each other. Indeed, this is true in most of the regions at depth 10 m, as seen in Fig. 22. Of particular interest are the two distinct positive regimes of $F_{K_n^0}$. They are related to the two barotropic transfer centers.

It merits notation that there is a strong negative regime in the top-left corner of Fig. 22c. Recall that in discussing the large-scale energy distribution (cf. Fig. 13), we have identified a large kinetic energy center in this place. Different from the two instability modal centers, we cannot identify a correspondence on the transfer maps. Now it is clear that this kinetic energy patch is highly related to the wind, and is therefore not due to intrinsic reasons.

To summarize, the large-scale MS-EVA balance is mainly between the the external forcing and the advective work together with the pressure work. Both the baroclinic transfer and the barotropic transfer are highly correlated to the wind, but the correlations in the two distinct transfer centers are quite different. The Point Sur mode is excited directly by the wind, while the Bay mode is due to a loss of balance established as the wind builds up. The latter provides an example of excitation of real ocean motion through storing energy first within large-scale window and then releasing it to form mesoscale processes.

9 Some observations about the sub-mesoscale processes

According to the previous spectral analysis, processes with scales less than half a day belong to the sub-mesoscale window. Sub-mesoscale processes are observed to be active for this region. In this study, however, it is difficult to investigate them on the sub-mesoscale window. The original simulation was generated such that observational data are assimilated on a daily basis. Daily processes are interfered with by the assimilation scheme, and a direct analysis

of the sub-mesoscale energetics therefore could not be reliable.

Nevertheless, we may still gain some understanding about the sub-mesoscale physics through investigating the transfers between the mesoscale window and the sub-mesoscale window. Transfer processes serve as a protocol between different scale windows, and as we did before, they can always be computed based on the larger window. In this case, we need only examine the mesoscale window (large-submesoscale transfer is much smaller).

We first discuss the simple case. In deep layers such as level 12 (150 m), the sub-mesoscale processes are rather weak (figures not shown). We just give a brief description here. On the maps of $T_K^{1\to 2}$, the significant transfer occurs in a region just near Point Ano Nuevo, particularly after the relaxation. On the $T_A^{1\to 2}$ maps, the transfer is limited within the bay. Generally speaking, it is positive before August 20, and after that it turns into negative. Recall that mesoscale thermal structures are generated at this level within the bay all the time through the experiment. The negative $T_A^{1\to 2}$ means that, although deriving their energy mainly from the large-scale background, these mesoscale structures after August 20 may also have a partial energy source from the sub-mesoscale processes.

The sub-mesoscale processes on the surface levels are more interesting. Contoured in Fig. 23 is a snapshot of the second level (10 m) energy transfers from the mesoscale window to the sub-mesoscale window. Both the APE (left) and KE (right) demonstrate a cascade of energy toward smaller scales on this day (August 15). This trend persists on the KE transfer map as of August 21, when it becomes more complicated. On the APE transfer map, the distribution is similar, except that a negative center moves in from southwest when the wind relaxes (figure not shown).

Compared to Figs. 15 and 16, Fig. 23 shows that a secondary instability follows the primary instability between the large-scale and mesoscale windows, releasing energy to sub-mesoscale processes. This secondary instability exhibits itself in a type mixed with baroclinicity and barotropicity. If observing closely the day-10 (August 15) pattern, one finds it actually sitting in a location bridging the Bay mode and the Point Sur mode on the maps of Fig. 16 and 15. That is to say, the energetic scenario here may be described as two primary instabilities within the bay and west of Point Sur, followed by a secondary instability lying in between.

10 Summary and conclusions

The multiscale dynamics of the August 2003 circulation in the Monterey Bay region has been investigated using the multiscale energy and vorticity analysis (MS-EVA) and the MS-EVA-based localized instability theory. The whole system is found to be governed by a bimodal instability structure, with two instabilities at two distinct locations. We have studied how the wind instills energy into the ocean to drive this structure.

The Monterey Bay system is found well organized in space and windowed in (time) scales. It can be roughly classified into two dynamically different types: a surface type and a deep type. During the experiment period, two regimes have been identified as intrinsic sources of the complicated surface flow system. Represented on the MS-EVA maps these regimes are two positive centers of baroclinic and barotropic perfect transfers (resp. BC and BT) from the large-scale window to the mesoscale window as constructed. They are located near the bay and offshore Point Sur, respectively, and has been since termed as the Bay mode and the Point Sur mode for convenience.

The two instability modes in the surface layers have different driving mechanisms lying behind. We have correlated the BC and BT in these two regimes to the wind. Both the correlations are very high, but the responses are opposite. A conclusion drawn from the observation is that the bimodal structure results from the wind, perhaps in cooperation with the coastal geometry. The difference between the two modes is that outside Point Sur the wind destablizes the system directly, while near the bay, the wind tends to stablize the southward coastal current, and instability occurs when the external constraint is relaxed.

Corresponding to the energy transfers toward the mesoscale window are the mesoscale fields. The mesoscale temperature and flow are found to be trapped above 200 m during the experiment, with a maximum near the thermocline. The potential and kinetic energy transfers generally correspond in timing to the mesoscale temperature and velocity respectively, though sometimes discrepancy in location does exist. We observed that a remarkable cooling during the wind recession on August 19. It is clearly not driven directly by the wind, nor from a remote region via wave propagation; rather it is caused by the local baroclinic instabilities. We have found the bay is a source region of perturbation. Disturbances are generated all the time during the experiment, and the generated disturbances propagate northward along the coast, in a form similar to the thermocline trapped mode of coastal trapped waves. Fig. 24 presents a cartoon summarizing the major physical processes in the surface layer.

The large-scale and mesoscale dynamics for the Monterey Bay circulation have distinct vertical structures. We have conducted a study for the deep flow

(below the thermocline), which is dynamically much simpler than its surface counterpart. During the experiment period, the bay is found baroclinically unstable all the time, which forms the only hotspot on the maps of large-to-mesoscale APE transfer. The corresponding large-to-mesoscale KE transfer is slightly different. The flow is barotropically unstable in the middle of the domain, starting from August 11 through the end of wind relaxation (August 23). Attached to the north is a negative transfer (stable regime), while to the south is another unstable center just outside Point Sur. The barotropic unstable center is found to be related to the submarine valley.

We have also examined the sub-mesoscale processes, based on the information available from the perfect transfers from the mesoscale window to the sub-mesoscale window. During August 15 through August 21, a secondary instability is identified in the surface layer from the clear and simple pattern of meso-to-sub-mesoscale transfer lying between the Bay and the southwestern corner. This pattern holds for both the potential energetics and the kinetic energetics, and the secondary instability is thereby of a mixed type. For the deep flow, a remarkable observation is that near the bay the transfer is negative after the wind relaxes toward the end of the month. That is to say, the deep layer mesoscale flow is not only fueled by the large-scale flow via instabilities, but also has its source derived from the sub-mesoscale processes.

We close the paper by remarking that this study shows an avenue how winds can excite the ocean through building up energy in the large-scale background, and then releasing it upon relaxation to fuel mesoscale eddies. We have also learned that a sudden cooling in the coastal ocean does not need to be directly driven by the wind, nor a result of remote cooling via wave propagation. It could be driven by a local instability process occurring *in situ*.

Acknowledgments

The simulation upon which this dynamical study is based is the collaborative reanalysis of the AOSN-II August 2003 Monterey Bay circulation performed by the Harvard Ocean Modeling Group, led by Dr. Patrick J. Haley, Jr., who provided the Harvard Ocean Prediction System output. We appreciate Wayne Leslie's help with the buoy and wind data. The authors acknowledge with gratitude the data-gathering efforts of the following scientists during AOSN- II: Dr. Francisco Chavez, Dr. Russ Davis, Dr. David Fratantoni, Dr. Steven Haddock, Dr. Margaret McManus, Dr. Erika McPhee-Shaw, and Dr. Steven Ramp. XSL also thanks Dr. Pierre Lermusiaux for several important discussions on the underlying dynamical processes. This work was supported by the Office of Naval Research under grants N00014-02-1-0989 and N00014-97-1-0239 to Harvard University.

A Coastal trapped waves in the Monterey Bay region

We have computed the free coastal trapped waves for three cross-shelf sections for the Monterey Bay region. (They are similar in result.) One section is outside Point Ano Nuevo, where wave propagations are frequently observed during the AOSN-II experiment. The topography is slightly modified, as marked in Fig. A.1a. The basic buoyancy frequency, which is shown in Fig. A.1b, is computed from the density profile averaged over all the available simulated density data on the section through the experiment. The eigenvalue problem is formed and solved with the method by Brink (1980, 1991), Clarke and Gorder (1986), and Wilkin and Chapman (1987). The eigenfunction of the thermocline-trapped mode is shown in Fig. A.2, which corresponds to a phase celerity of 0.9 ms^{-1}.

References

[1] Abraham, R. and Jerrold E. Marsden, 1981: *Foundations of Mechanics.* Perseus Publishing.

[2] Bigelow, H. B., and M. Leslie, 1930: Reconnaissance of the waters and plankton of Monterey Bay, July, 1928. *Bulletin of the Museum of Comparative Zoology at Harvard College* 70, 427-581.

[3] Breaker, L. C., and W. W. Broenkow, 1994: The cirulation of Monterey Bay and related processes. In: *Oceanography and Marine Biology: an Annual Review* 32, 1-64. A. D. Ansell, R. N. Gibson and M. Barnes, Eds., UCL Press.

[4] Breaker, L. C., and C. N. K. Mooers, 1986: Oceanic variability off the central California coast. *Prog. Oceanogr.* 17, 61-135.

[5] Brink, K. H., 1980: Propagation of barotropic continental shelf waves over irregular bottom topography. *J. Phys. Oceanogr.*, 10, 765-778.

[6] Brink, K. H., 1991: Coastal-trapped waves and wind-driven currents over the continental shelf, *Annu. Rev. Fluid Mech.*, 23, 389-412.

[7] Chelton, D. B., A. Bratkovch, R. L. Bernstein, and P. M. Kosro, 1988: The polewardflow off central California during the spring and summer of 1984. *J. Geophys. Res.*, 93, 10604-10620.

[8] Clarke, A., and van Gorder, 1986: A method for estimating wind-driven frictional, time-dependent, and stratified shelf and slope water flow. *J. Phys. Oceanogr.*, 16, 1013-1028.

[9] Collins, C. A., N. Garfield, T. A. Rago, F. W. Rischmiller, and E. Carter, 2000: Mean structure of the inshore countercurrent and California undercurrent off Point Sur, California. *Deep-Sea Res.*, Part II, 47, 765-782.

[10] Dewery, R. K., J. N. Moum, C.A. Paulson, D. R. Caldwell, and S. D. Pierce, 1991: Structure and dynamics of a coastal filament. *J. Geophys. Res.*, 90, 4741-4755.

[11] Griggs, G. B, 1974: Nearshore current patterns along the central California coast. *Est. & Coast. Mar. Sci.* 2, 395-405.

[12] Kelly, K. A., 1985: The influence of winds and topography on the sea surface temperature patterns over the northern California slope. *J. Geophys. Res.*, 90, 1655-1681.

[13] Lermusiaux, P. F. J., 2005: Real-time error prediction and data assimilation with ESSE. (this volume)

[14] Liang, X. S., 2002: Wavelet-based multiscale window transform and energy and vorticity analysis. *Harvard Reports in Physical/Interdisciplinary Ocean Science*, Rep. No. 66, Harvard University, Cambridge, MA. 411 pp.

[15] Liang, X. S., and A. R. Robinson, 2004: A study of the Iceland-Faeroe frontal variability using the multiscale energy and vorticity analysis. *J. Phys. Oceanogr.*, 34, 2571-2591.

[16] Liang, X. S., and A. R. Robinson, 2005a: Localized multiscale energy and vorticity analysis. I. Fundamentals. *Dyn. Atmos. Oceans*, 38, 195-230.

[17] Liang, X. S., and A. R. Robinson, 2005b: Localized multiscale energy and vorticity analysis. II. Instability theory and validation. *Dyn. Atmos. Oceans* (in press).

[18] Narimousa, S., and T. Maxworthy, 1989: Application of a laboratory model to the interpretation of satellite and field observations of coastal upwelling. *Dyn. Atmos. Oceans*, 13, 1-46.

[19] Pringle, J. M., and Kristin Riser, Remotely forced nearshore upwelling in Southern California. *J. Geophs. Res.* (in press).

[20] Ramp, S. R., L. K. Rosenfeld, T. D. Tisch, and M. R. Hicks, 1997: Moored observations of the current and temperature structure over the continental slope off central California. 1. A basic description of the variability, *J. Geophys. Res.*, 102, 22,877-22,902.

[21] Haley, P. J., et al., 2005: Real-time forecasting and re-analysis fields of the Monetary Bay circulation. (this volume)

[22] Rosenfeld, L. K., F. B. Schwing, N. Garfield, and D. E. Tracy, Bifurcation flow from an upwelling center: A cold water source for Monterey Bay, *Cont. Shelf Res.*, 14, 931-964, 1994.

[23] Shepard, F. P., R. Revelle, and R. S. Dietz, 1939: Ocean-bottom currents off the California coast. *Sci.* 89, 488-489.

[24] Skogsberg, T., 1936: Hydrography of Monterey Bay, California. Thermal conditions, 1929-1933. *Trans. Amer. Phil. Soc.*, 29, 152 pp.

[25] Strub, P. T., J. S. Allen, A. Huyer, and R. L. Smith, 1987: Seasonal cycles of currents, temperatures, winds, and sea level over the northeast Pacific continental shelf: 35N to 48N. *J. Geophys. Res.*, 92, 1507-1526.

[26] Wilkin, J. L., and D. C. Chapman, 1987: Scattering of continental shelf waves at a discontinuity in shelf width. *J. Phys. Oceanogr.*, 17, 713-724.

Table Captions

Table 1
Symbols for multiscale energetics (time step n, scale window ϖ). For details, refer to Liang and Robinson (2005).

Kinetic energy (KE)		Available potential energy (APE)	
$\dot{K}_n^{\varpi}$	Time rate of change of KE	$\dot{A}_n^{\varpi}$	Time rate of change of APE
$\Delta Q_{K_n^{\varpi}}$	KE advective working rate	$\Delta Q_{A_n^{\varpi}}$	APE advective working rate
$T_{K_n^{\varpi}}$	Total KE transfer	$T_{A_n^{\varpi}}$	Total APE transfer
$\Delta Q_{P_n^{\varpi}}$	Pressure working rate	b_n^{ϖ}	Rate of buoyancy conversion
$F_{K_n^{\varpi},z}$	Rate of vertical dissipation	$F_{A_n^{\varpi},z}$	Rate of vertical diffusion

Table 2
Parameters for the application of MS-EVA.

Parameters	Value
Time window bounds: j_0, j_1	2, 6 (8, 0.5 days)
Space window bound: j_0^{sp}	5 ($\sim$11 km)
$\bar{\rho}(z)$	See Fig. 6
Grid	$83 \times 96 \times 22$
Time stepsize Δt	3 hrs
Horizontal grid spacing Δx, Δy	1.5 km
Vertical level depths (levels 1-22, in meters):	
2.5, 10, 20, 30, 40, 50, 60,	
72.5, 90, 110, 130, 150, 170, 202.5,	
250, 300, 350, 400, 450, 500, 550, 600	

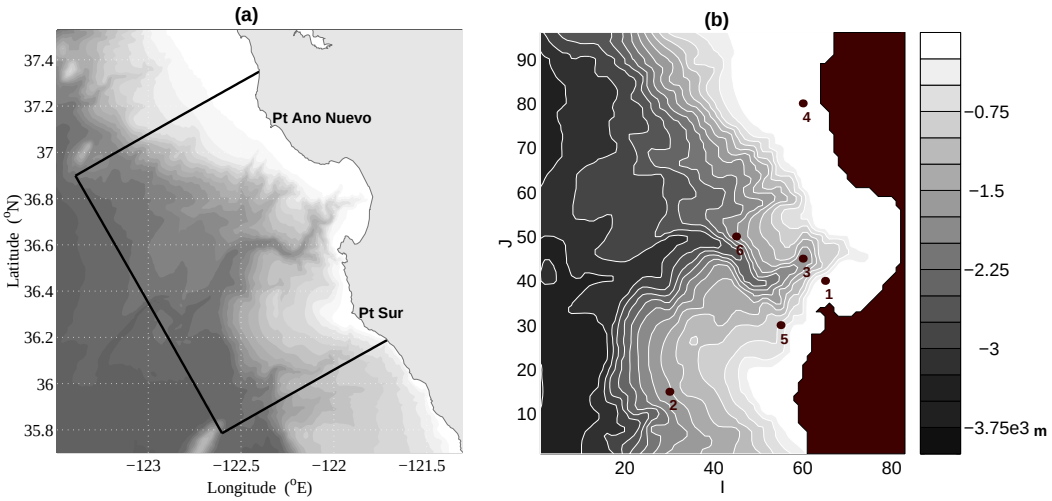

Fig. 1. (a) Research domain for the AOSN-II experiment. Marked are the two locations referred in the text: Point Ano Nuevo and Point Sur. (b) The enlarged and rotated (by 30^o clockwise) domain overlaped with bottom topography (depth in meters). Also shown are the six locations where time series are extracted for spectral analysis. The coordinates are grid point indices.

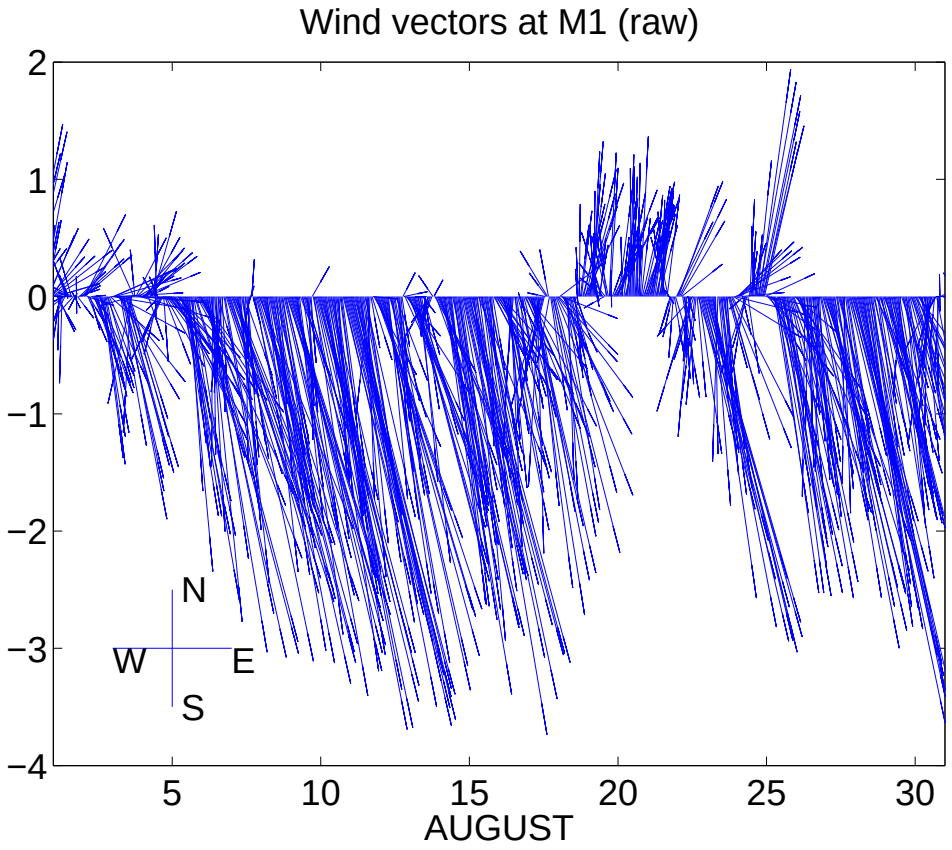

Fig. 2. Stickplot of the wind (in knots) at M1 (36.755^{o}N, 122.025^{o}W) during the period of AOSN-II experiment.

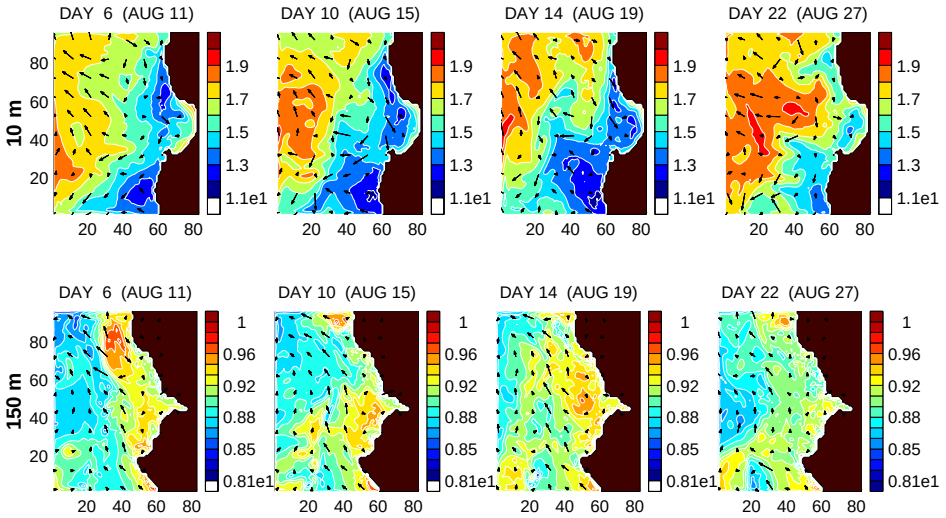

Fig. 3. Sequence of simulated temperature for depths 10 m (top) and 150 m (bottom).

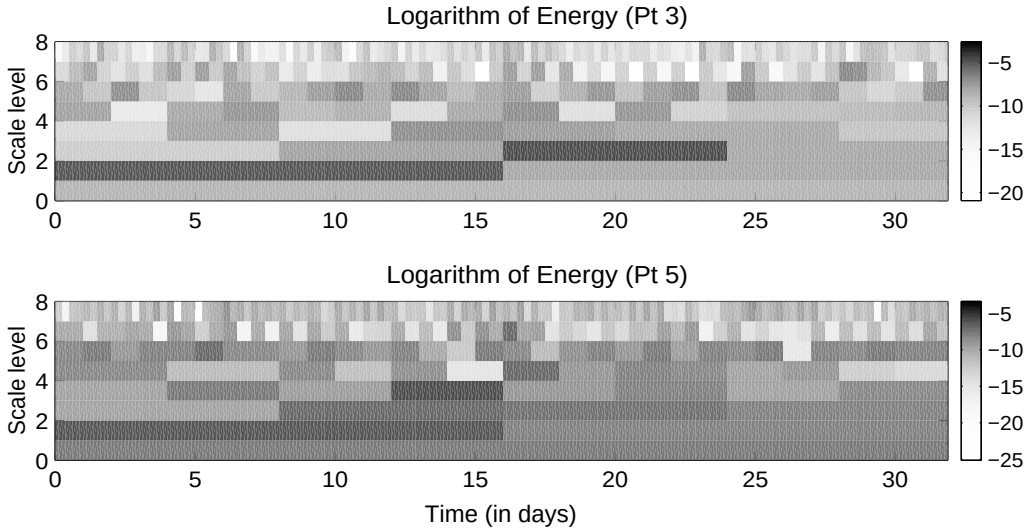

Fig. 4. Wavelet energy spectrum for the surface temperature time series at points 3 (top) and 5 (bottom). Shown here are the logarithms of the wavelet transform coefficients squared. The transform is with an orthonormalized cubic spline basis (cf. LR1 and LR3). The scale level j is defined such that 2^{-j} is equal to the time scale normalized by the duration (here 32 days).

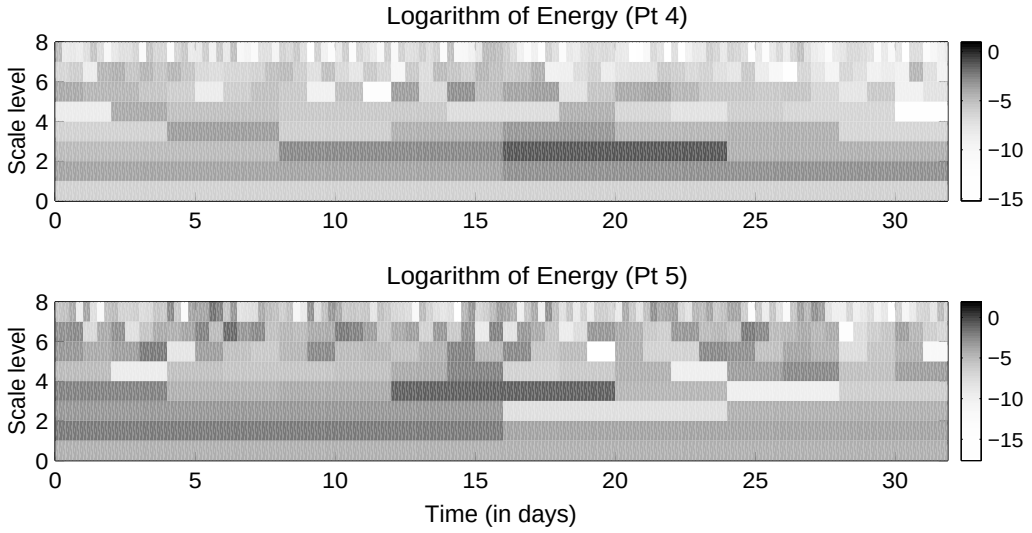

Fig. 5. Spectral analysis for the surface x-velocity at points 4 (top) and 5 (bottom).

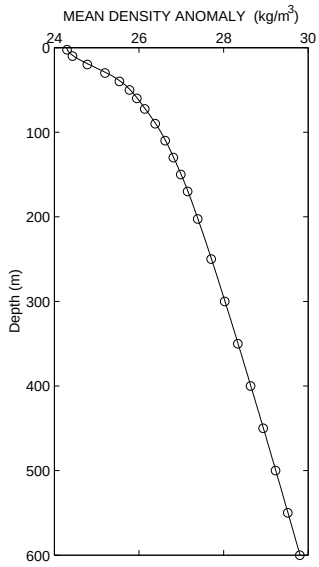

Fig. 6. Profiles of mean density anomaly $\bar{\rho} = \bar{\rho}(z)$.

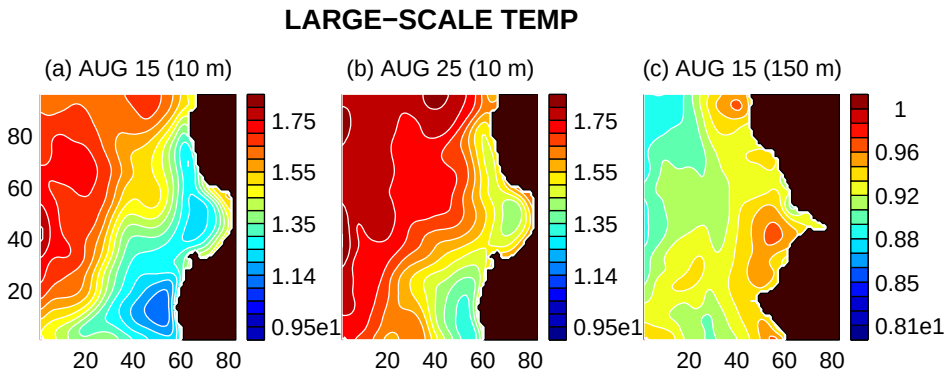

Fig. 7. Large-scale temperature for depths 10 m and 150 m.

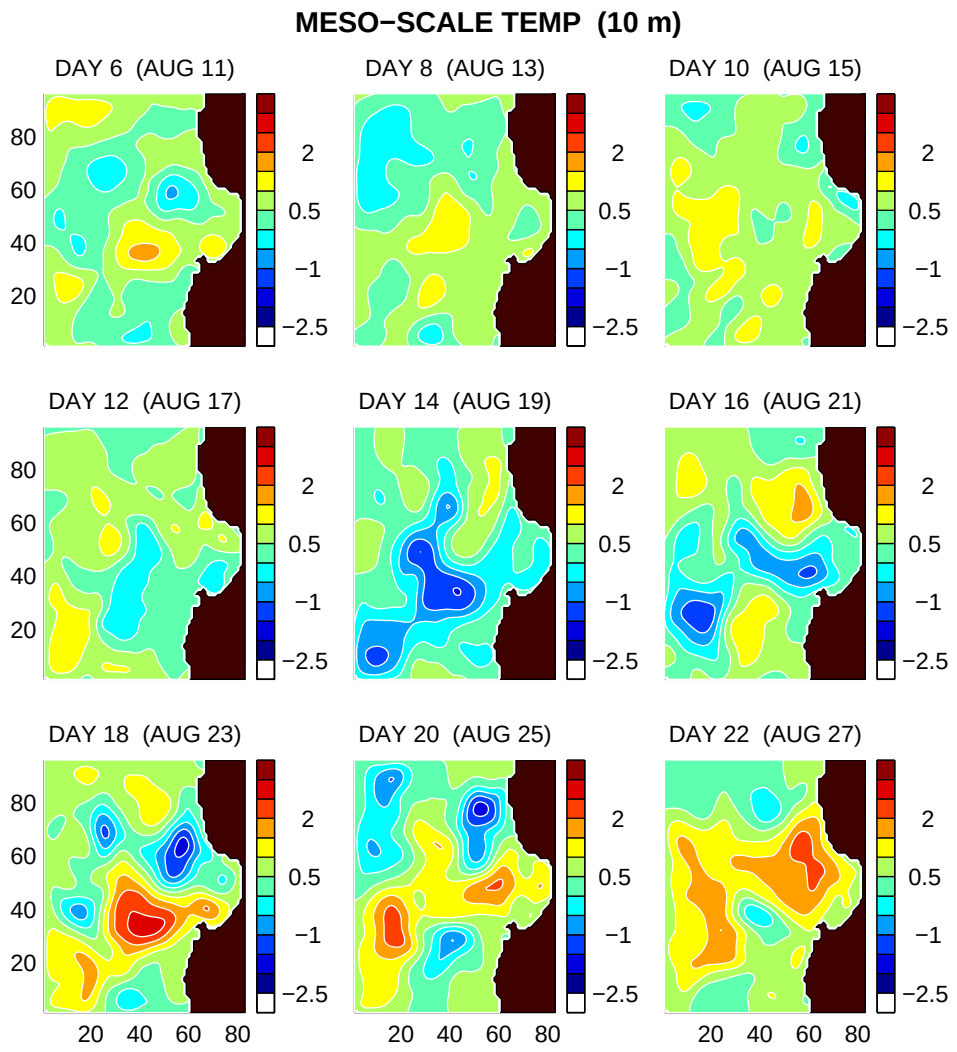

Fig. 8. Sequence of meso-scale temperature at depth 10 m.

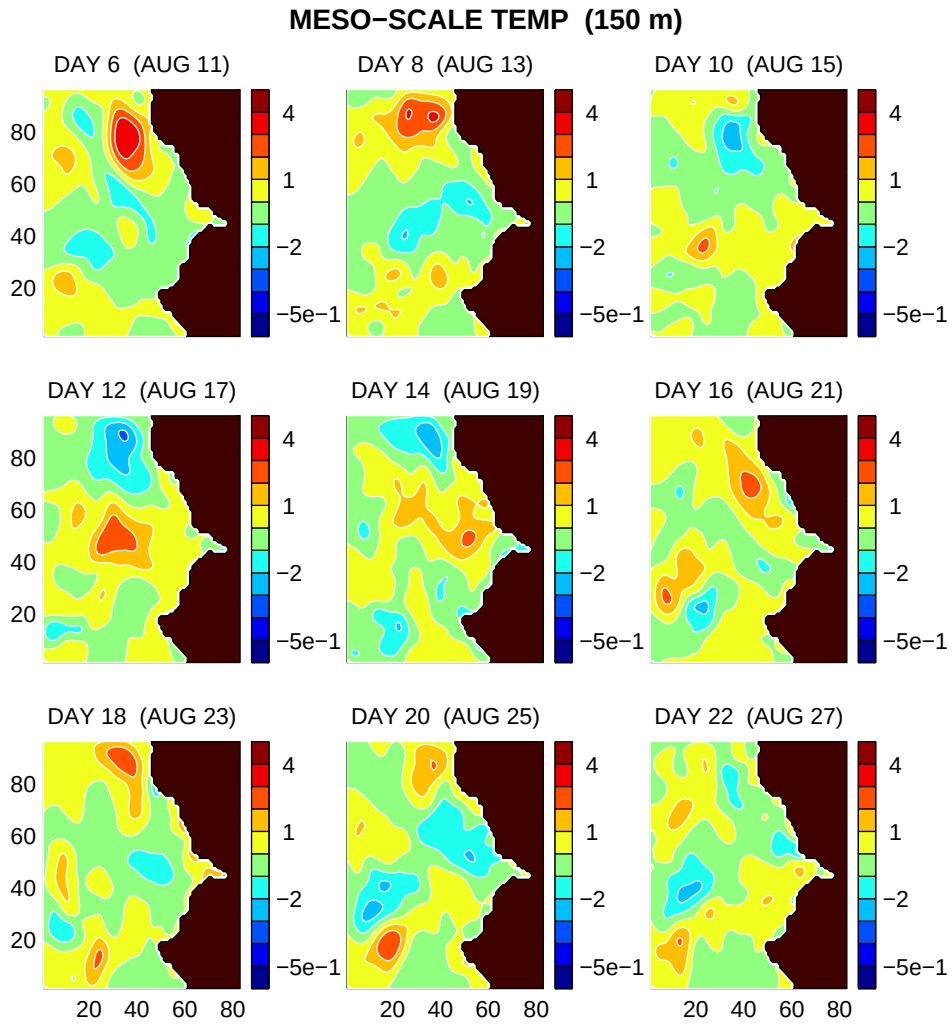

Fig. 9. Sequence of meso-scale temperature at depth 150 m.

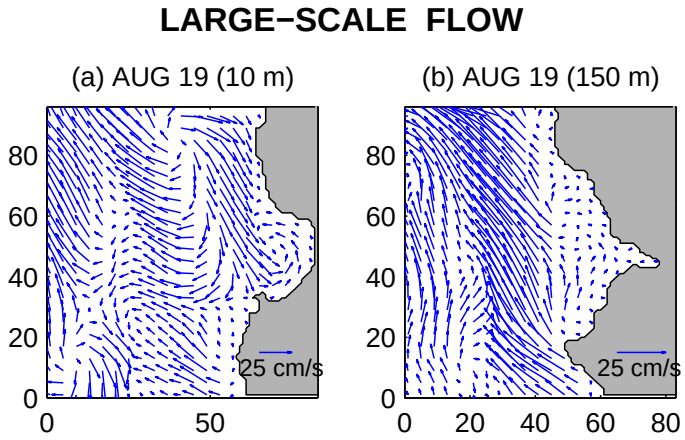

Fig. 10. Large-scale velocity for (a) depth 10 m and (b) depth 150 m.

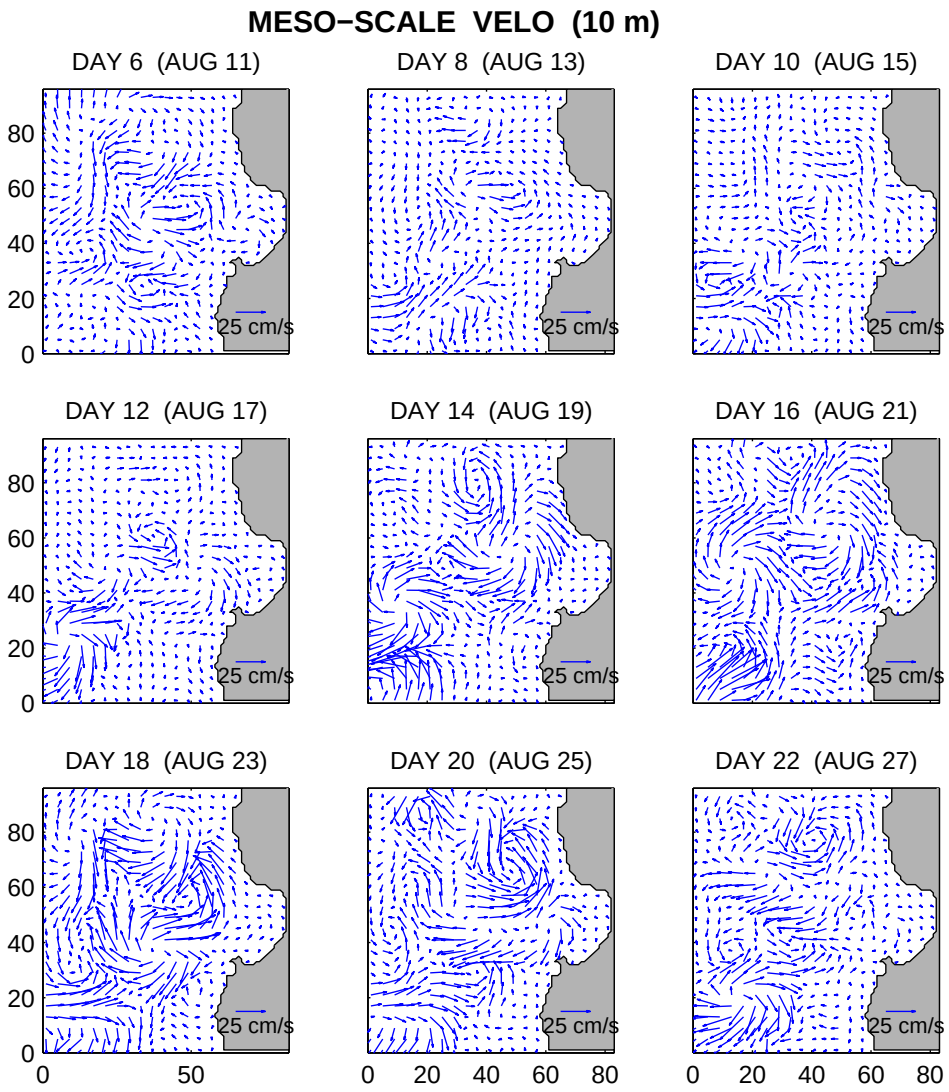

Fig. 11. Sequence of meso-scale velocity at depth 10 m.

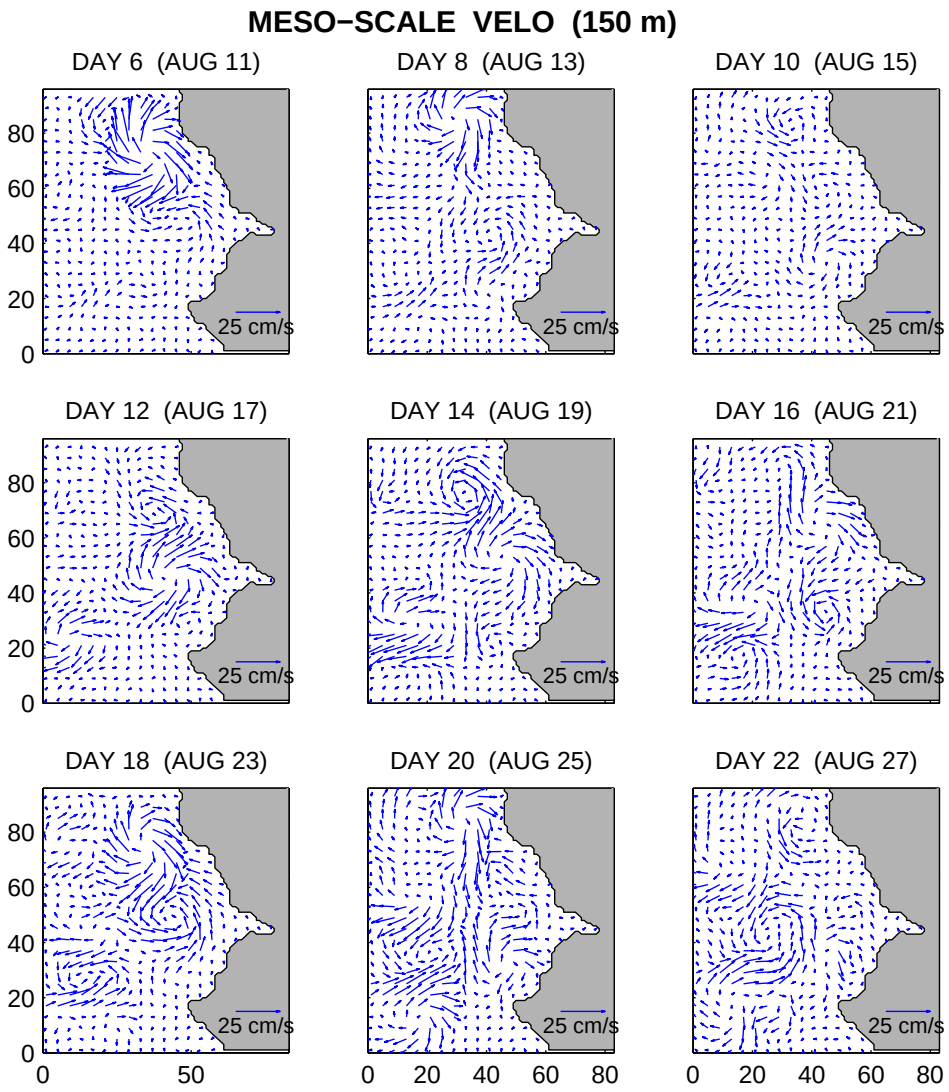

Fig. 12. Sequence of meso-scale velocity at depth 150 m.

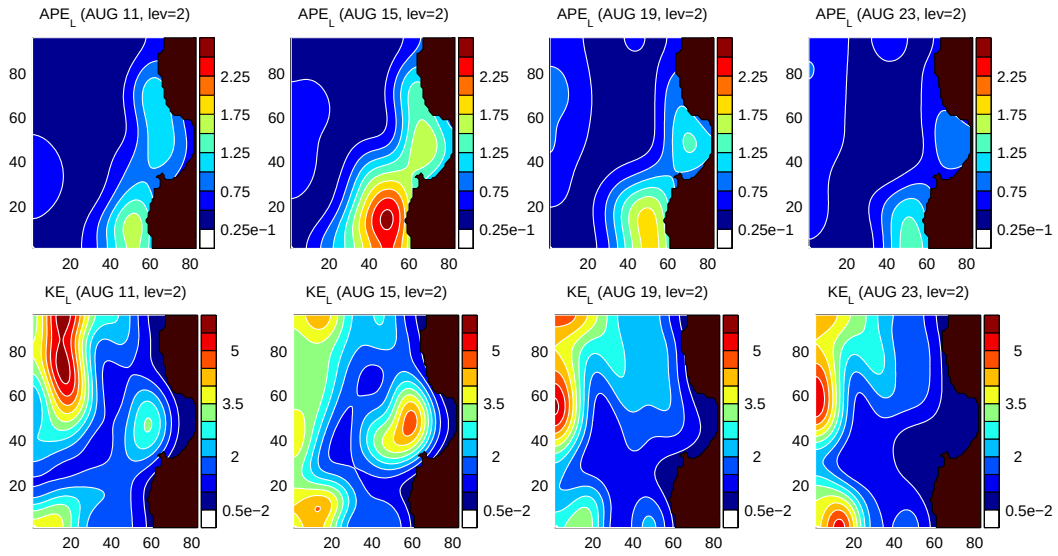

Fig. 13. A time sequence of large-scale available potential energy (upper panel) and kinetic energy (lower panel) for level 2 (10 m). Note different scales for the colorbars.

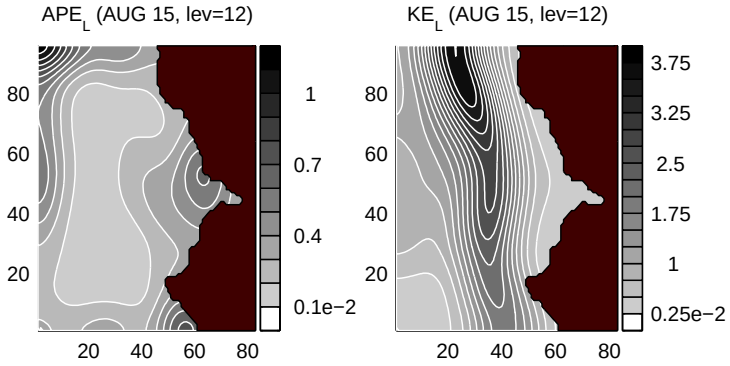

Fig. 14. Large-scale available potential energy (left) and kinetic energy (right) at level 12 (150 m) for August 15, 2003.

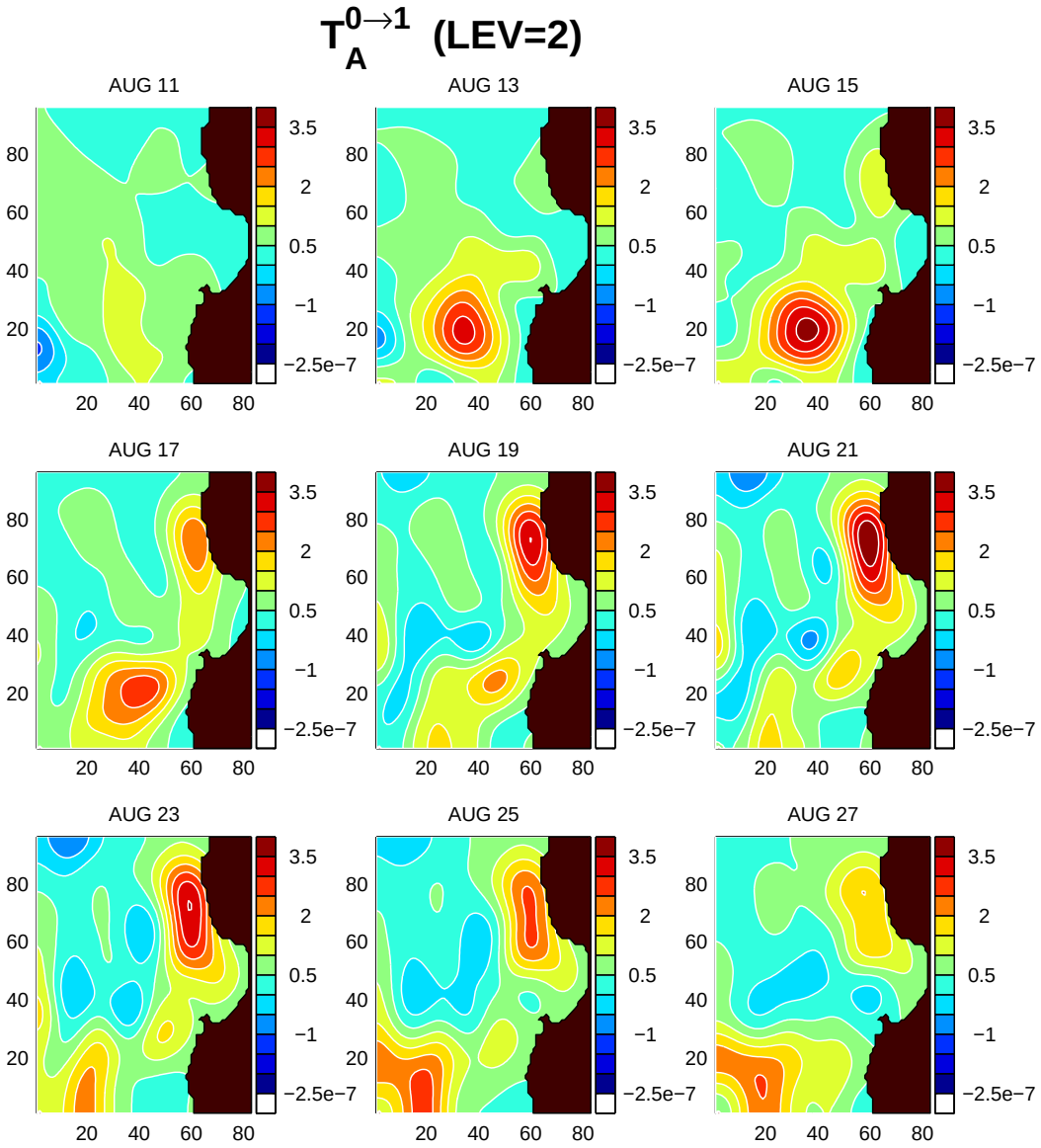

Fig. 15. Potential energy transfer (large-scale window based) at depth 10 m from large-scale window to meso-scale window (BC). (Units: m^2/s^3)

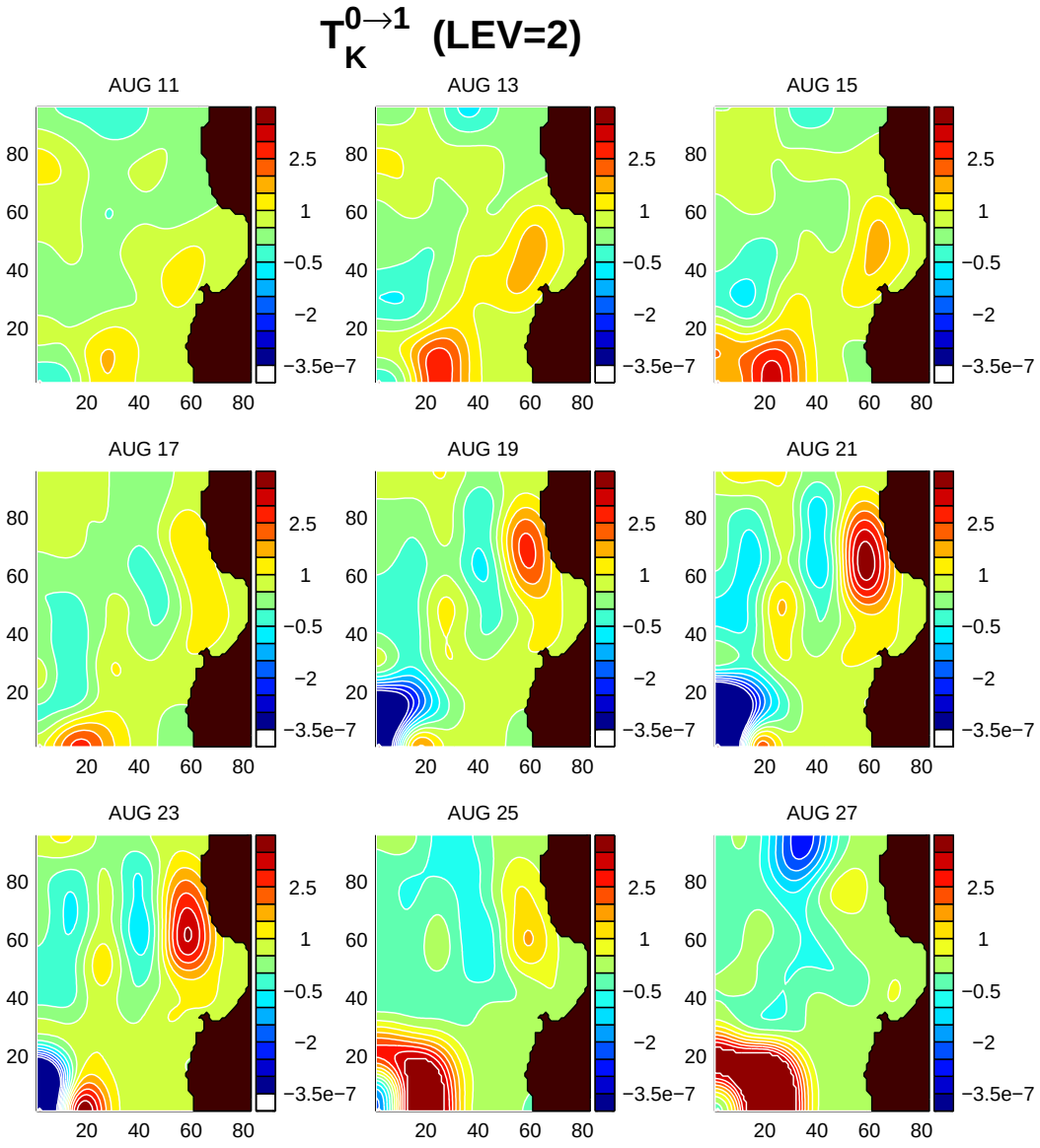

Fig. 16. Kinetic energy transfer (large-scale window based) at depth 10 m from large-scale window to meso-scale window (BT) (in m^2/s^3). For comparison purpose, contours with values exceeding $\pm 3.5 \times 10^{-7}$ are not drawn.

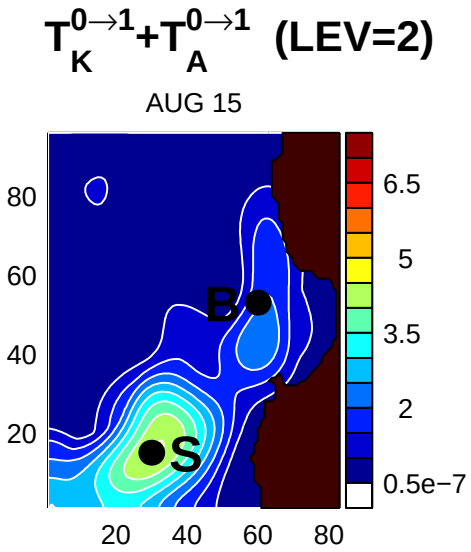

Fig. 17. BC + BT (in m^2/s^3) at depth 10 m for August 15. The two points, B(57,55) and S(30,15), are marked for use in section 8.

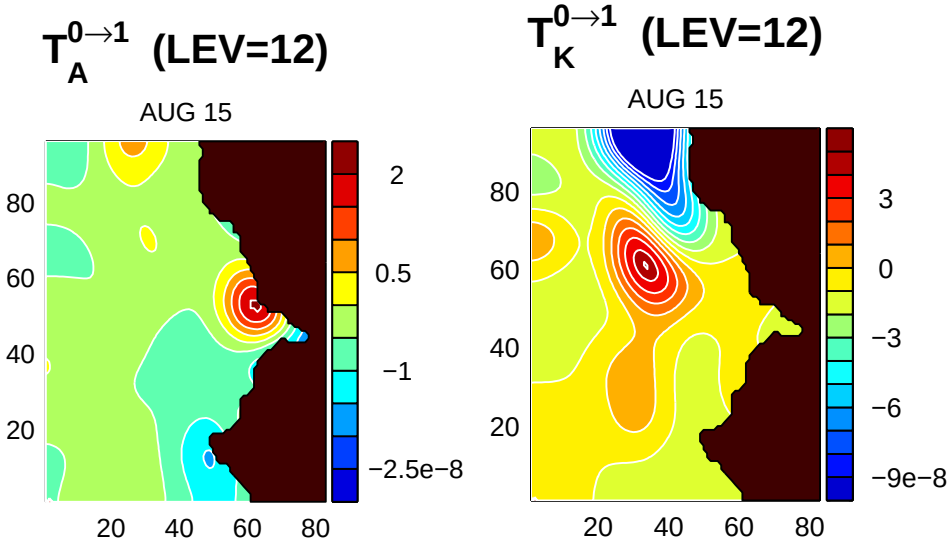

Fig. 18. Potential energy transfer (left) and kinetic energy transfer (right) at level 12 (150 m) from large-scale window to meso-scale window. (Units: m^2/s^3)

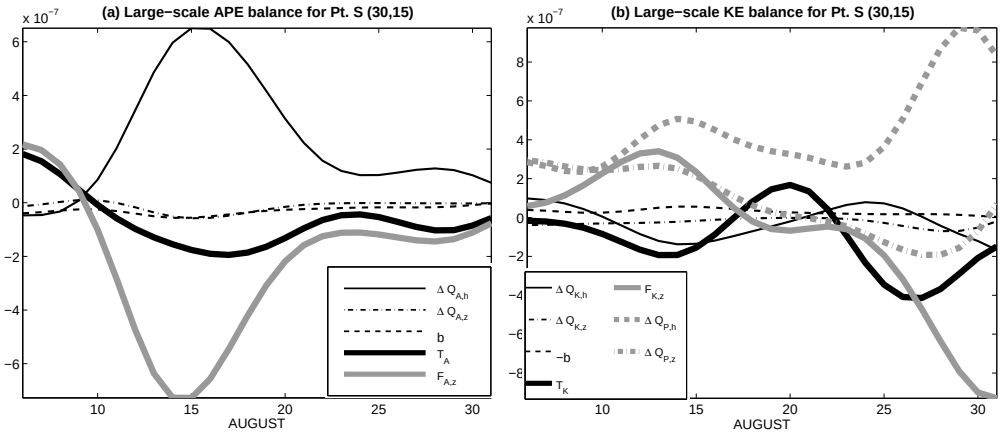

Fig. 19. Large-scale APE (a) and KE (b) balance for point S(30,15) at depth 10 m (cf. Fig. 17 for location). Inserted are the legends for the MS-EVA terms. The symbols are: $\Delta Q_{A,h}$: horizontal APE advection; $\Delta Q_{A,z}$: vertical APE advection; b: buoyancy conversion; T_A: total APE transfer; $F_{A,z}$: vertical diffusion; $\Delta Q_{K,h}$: horizontal KE advection; $\Delta Q_{K,z}$: vertical KE advection; $\Delta Q_{P,h}$: horizontal pressure work; $\Delta Q_{P,z}$: vertical pressure work; T_K: total KE transfer; $F_{K,z}$: vertical dissipation; They are the same as listed in Table 1 but with time location index n and window index ϖ removed ($\varpi = 0$ here) for clarity.

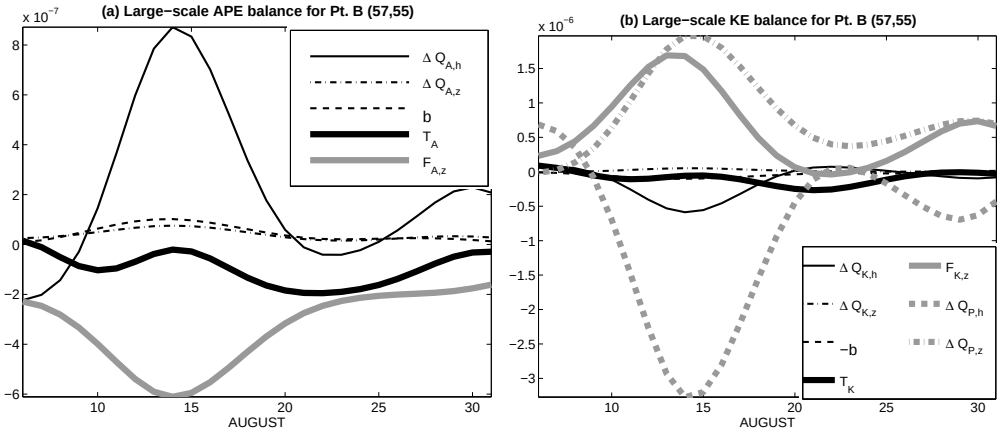

Fig. 20. Same as Fig. 19, but for point B(57,55).

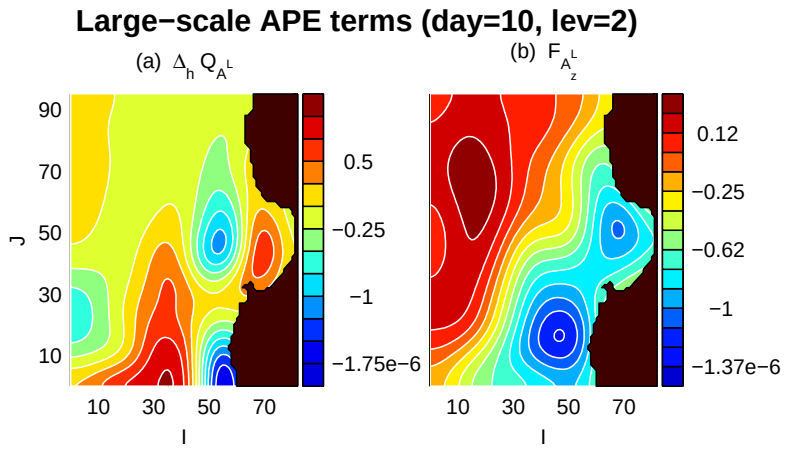

Fig. 21. Large-scale potential energy balance at the second level (10 m) on August 15 (units: m^2/s^3).

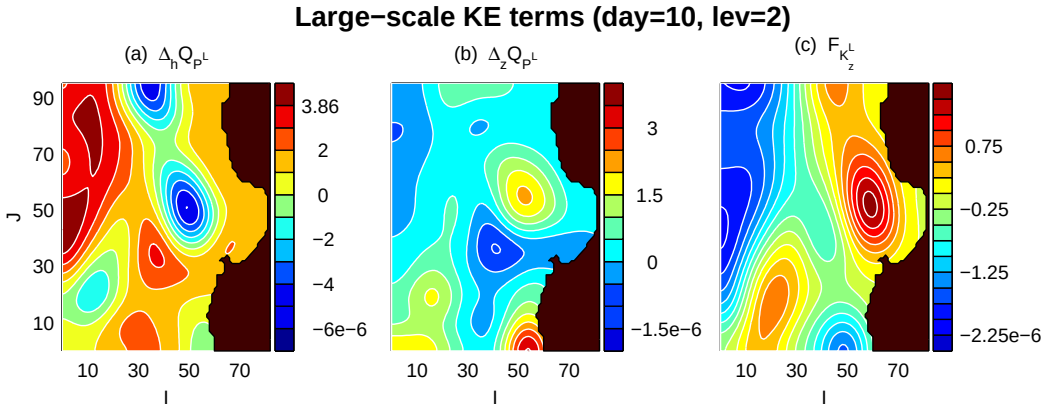

Fig. 22. Large-scale kinetic energy balance at the second level (10 m) on August 15 (units: m^2/s^3).

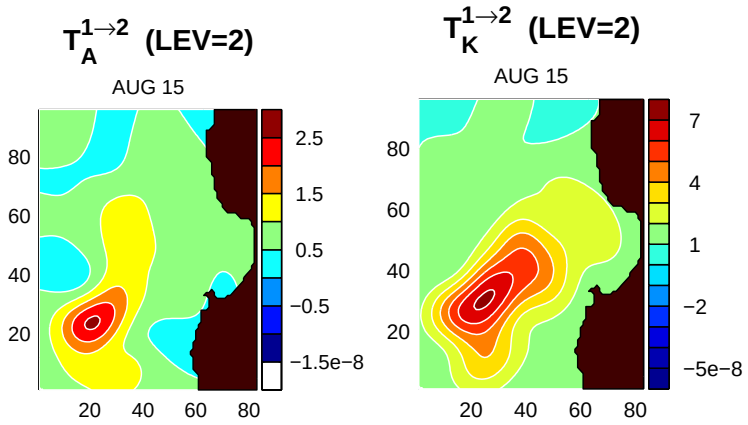

Fig. 23. Potential energy transfer (left panel) and kinetic energy transfer (right panel) between meso- sub-meso-scale windows on August 15 for depth 10 m (units: $m^2 s^{-3}$). Positive value indicate a transfer from the meso-scale window to the sub-mesoscale window.

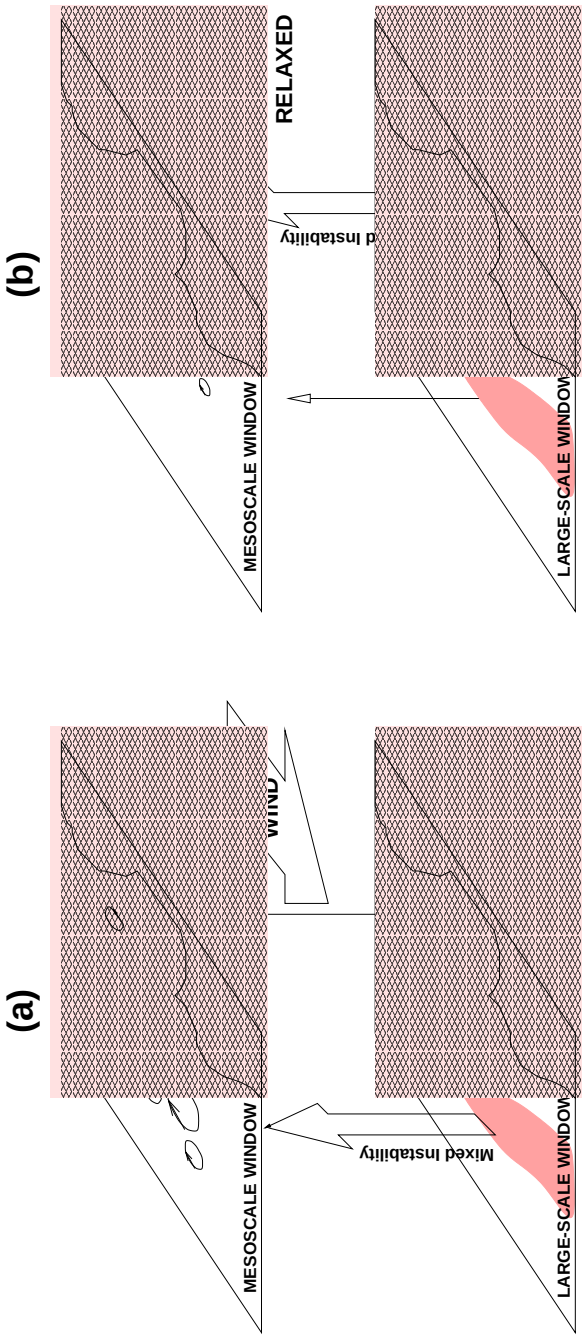

Fig. 24. A cartoon summarizing the major dynamical processes in the upper layer of the Monterey Bay. Two modes of instability, both of mixed type, are identified near the bay and outside Point Sur, respectively. The Point Sur mode (a) is stronger when the southwestward wind applies, while the bay mode (b) results mainly from the relaxation of the wind. The generated mesoscale events propagate northward in the form of coastal trapped waves (CTW).

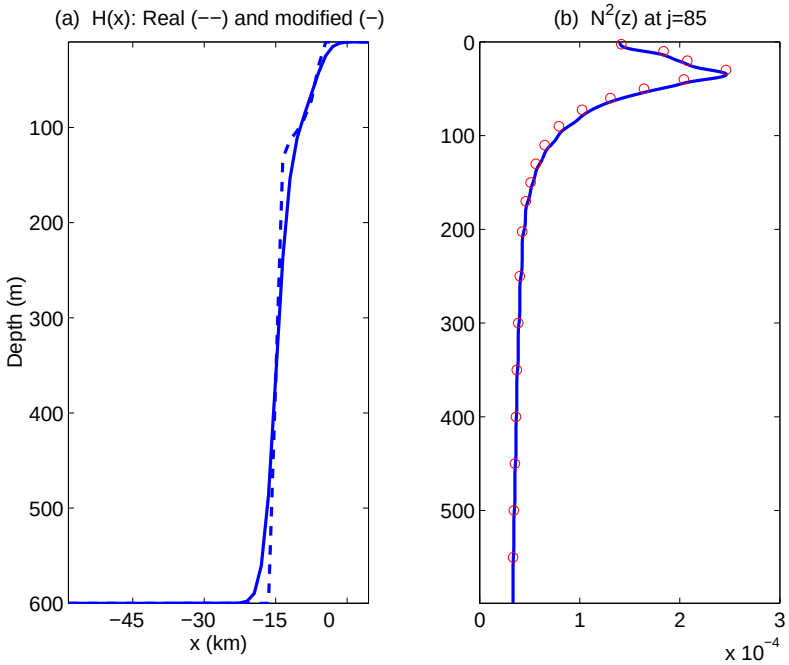

Fig. A.1. (a) Topography and (b) buoyancy frequency profiles for the coastal trapped waves computation.

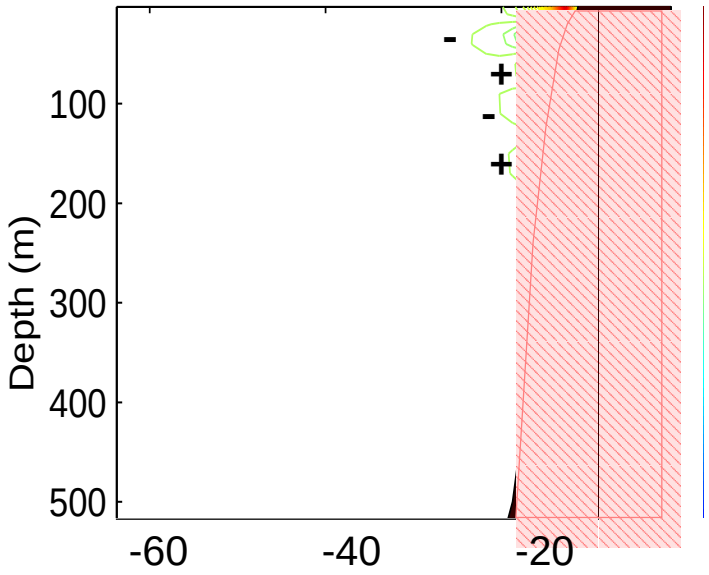

Fig. A.2. The thermocline trapped mode of the coastal trapped waves in the Monterey Bay region. It corresponds to an eigenvalue (1/c) of 11 m^{-}1s ($c \approx 0.09$ m/s). The signs "+" and "−" indicate the positive and negative regions of contour lines.